Quasiparticle interference on the surface of the topological insulator Bi_2Te_3

Wei-Cheng Lee,[1] Congjun Wu,[1] Daniel P. Arovas,[1] and Shou-Cheng Zhang[2]
[1]*Department of Physics, University of California, San Diego, California 92093, USA*
[2]*Department of Physics, McCullough Building, Stanford University, California 94305, USA*
(Received 10 October 2009; revised manuscript received 24 November 2009; published 29 December 2009)

The quasiparticle interference of the spectroscopic imaging scanning tunneling microscopy has been investigated for the surface states of the large gap topological insulator Bi_2Te_3 through the *T*-matrix formalism. Both the scalar-potential scattering and the spin-orbit scattering on the warped hexagonal isoenergy contour are considered. While backscatterings are forbidden by time-reversal symmetry, other scatterings are allowed and exhibit strong dependence on the spin configurations of the eigenfunctions at $\vec{k}$ points over the isoenergy contour. The characteristic scattering wave vectors found in our analysis agree well with recent experiment results.

DOI: 10.1103/PhysRevB.80.245439 PACS number(s): 68.37.Ef, 73.43.Cd

I. INTRODUCTION

The theoretical proposal[1–8] and experimental discovery of the topological insulators[9–12] have provoked an intensive research effort in condensed-matter physics. Topological insulators (TI) with time-reversal (TR) symmetry are generally characterized by a topological term in the electromagnetic action with a quantized coefficient.[4] These states have been theoretically predicted and experimentally observed in both two and three dimensions, including the two-dimensional (2D) HgTe/HgCdTe quantum wells,[1,9] and bulk three-dimensional (3D) materials Bi_2Te_3, Bi_2Se_3, and $Bi_{1-x}Sb_x$.[5,8,10–13] They exhibit robust gapless modes at boundaries, e.g., a one-dimensional (1D) helical edge mode for 2D TIs and a 2D helical surface mode for 3D TIs with odd numbers of Dirac cones. Due to time-reversal symmetry, backscattering is forbidden for the helical edge and surface states, and an analysis of interaction effects for the 1D helical edge modes shows they are stable against weak and intermediate strength interactions.[14,15] Bi_2Te_3 and Bi_2Se_3 have been predicted to have bulk band gaps exceeding room temperature,[8] which makes them promising for future applications.

Zhang *et al.*[8] predict that the surface states of Bi_2Te_3 consist of a single Dirac cone at the Γ point, and that the Dirac cone evolves into a hexagonal shape at higher energy. Furthermore, near the Dirac point, the spin of the electron lies perpendicular to the momentum. Angle-resolved photoemission spectroscopy (ARPES) measurements performed on the surface of Bi_2Te_3 have confirmed these predictions in detail.[12,16] The typical shape of the Fermi surface is a snowflakelike warped hexagon. The low-energy O(2) symmetry of the Dirac cone is broken due to the C_{3v} symmetry of the underlying lattice[8] and can be modeled by a warping term in the effective model.[17] Another powerful surface probe, spectroscopic scanning tunneling microscopy (STM), is sensitive to quasiparticle interference (QPI) around impurities, and provides an important tool to study electronic structures in unconventional materials, such as high-T_c cuprates.[18,19] It can provide information in momentum space through real-space measurement with a high-energy resolution. Recently, several groups have performed STM measurements on surface states of Bi_2Te_3 and $Bi_{1-x}Sb_x$.[13,20–22] Backscattering induced by nonmagnetic impurities between TR partners with opposite momenta is forbidden due to their opposite spin configurations. This is confirmed by the real-space Friedel oscillation pattern and by analysis of the QPI characteristic scattering wave vector.

In this paper, we perform a detailed QPI analysis of the surface states of the topological insulator Bi_2Te_3. A general TR-invariant impurity potential including scalar and spin-orbit scattering components is studied using the standard *T*-matrix formalism. The scattering on the isoenergy surface strongly depends on the both momentum and spin orientation. Scattering between TR partners vanishes as a consequence of TR symmetry. The scattering is dominated by wave vectors which connect regions on the Fermi surface of extremal curvature but also accounting for spin polarization. STM experiments[20,21] have yielded rich information about the QPI structure. In addition to the absence of backscattering, the STM experiments also observed recovered scattering[20] at a wavevector ($\vec{k}_{\rm nest}$ in their, and $\vec{q}_2$ in our notation), and an extinction[21] (i.e., near absence of scattering) ($\vec{q}_3$ in their and our notation), both at wavevectors which do not connect TR states. Below, we offer an explanation of this experimental puzzle. Our results are in excellent overall agreement with the QPI experiment in Bi_2Te_3.

II. SURFACE DIRAC MODEL WITH WARPING TERM

The $\vec{k}\cdot\vec{p}$ Hamiltonian for the surface Dirac cone was first derived in Ref. 8. The bare Hamiltonian is written as $\mathcal{H}_0=\int d^2k\psi^\dagger(\vec{k})H(\vec{k})\psi(\vec{k})$, where $\psi^\dagger(\vec{k})=(c^\dagger_{\vec{k}\uparrow},c^\dagger_{\vec{k}\downarrow})$. With the addition of the cubic warping term,[17]

$$H(\vec{k})=v(\vec{k}\times\vec{\sigma})\cdot\hat{z}+\lambda k^3\cos 3\phi_{\vec{k}}\sigma^z. \quad (1)$$

The azimuthal angle of $\vec{k}$ is $\phi_{\vec{k}}=\tan^{-1}(k_y/k_x)$, where the Γ-K direction is taken as $\hat{x}$ axis. Following Ref. 17, the quadratic terms are dropped since they do not significantly change the shape of the constant energy contour, and the characteristic energy and wave-vector scales are defined as $E^*=v\ k_c$ and $k_c=\sqrt{v/\lambda}$. This Hamiltonian can be diagonalized by introducing

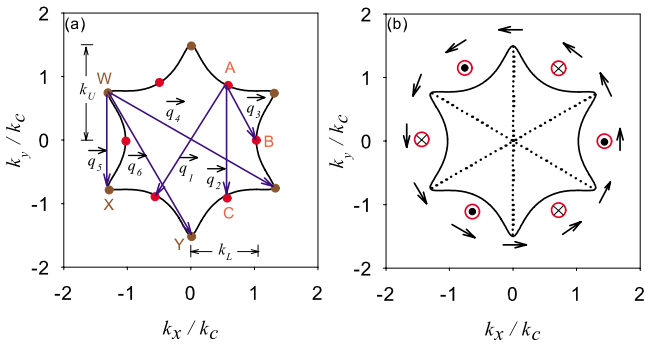

FIG. 1. (Color online) (a)The isoenergy contour near the Γ point for $E=1.5E^*$ with snow-flake shape. The $\hat{x}$ and $\hat{y}$ axes are chosen to be the Γ-K and Γ-M directions, respectively, and $k_c=\sqrt{v/\lambda}$. The red (gray) and brown (dark gray) dots refer to the valley and the tip points on the contour, and the arrows indicates six representative scattering wave vectors. k_L and k_U are solutions of $E_+(k_L,\theta=0)=E_+(k_U,\theta=\pi/2)=E$ which are the boundary of the truncation for the $\vec{k}$ integration used in this paper. (b) The spin orientations of the eigenfunctions for α_+ band at valley and tip points. The dotted lines refer to the mirror-symmetric lines (Γ-M), and the system has a threefold rotational symmetry. The arrow indicate the spin configuration in the xy plane and the solid circle (cross) refers to S_z being along $+\hat{z}(-\hat{z})$. At the cusp points the spin lies only on the xy plane while S_z has the largest magnitude at the valley points with staggered signs.

$$\hat{U}(\vec{k})=\begin{pmatrix}\cos(\theta_{\vec{k}}/2) & ie^{-i\phi_{\vec{k}}}\sin(\theta_{\vec{k}}/2)\\ ie^{i\phi_{\vec{k}}}\sin(\theta_{\vec{k}}/2) & \cos(\theta_{\vec{k}}/2)\end{pmatrix}, \tag{2}$$

where $\tan\theta_{\vec{k}}=k_c^2/(k^2\cos 3\phi_{\vec{k}})$. One then finds $H(\vec{k})=E(\vec{k})U(\vec{k})\sigma^z U^\dagger(\vec{k})$, with eigenvalues $E_\pm=\pm E(\vec{k})$, where

$$E(\vec{k})=\sqrt{(vk)^2+(\lambda k^3\cos 3\theta_{\vec{k}})^2}. \tag{3}$$

In Fig. 1(a) we plot the isoenergy contour $E=1.5E^*$, which qualitatively reproduces the snowflake Fermi surface observed in the first-principles calculation and the ARPES experiment.[8,12,17] As for the scattering process, we take

$$\mathcal{H}_{\rm imp}=\int d^2k d^2k' V_{\vec{k}-\vec{k}'}\psi^\dagger(\vec{k}')[\mathbb{I}+ic\vec{k}\times\vec{k}'\cdot\vec{\sigma}]\psi(\vec{k}). \tag{4}$$

For a single short-ranged scatterer we may approximate $V_{\vec{k}-\vec{k}'}\approx V_0$. The second term corresponds to the spin-orbit scattering with the coefficient c describing its relative strength to the potential scattering. It is convenient to project the potential onto the eigenbasis of $\mathcal{H}_0$ so

$$\hat{V}_{\vec{k},\vec{k}'}\equiv V_0\hat{U}^\dagger(\vec{k}')[\mathbb{I}+ic\vec{k}\times\vec{k}'\cdot\vec{\sigma}]\hat{U}(\vec{k}). \tag{5}$$

For simplicity, we first consider the $c=0$ case (pure scalar-potential scattering), returning later to the general spin-orbit case ($c\neq 0$). Since the spectrum is particle-hole symmetric, let us focus on a definite (positive) sign of the energy. The QPI will then be dominated by scatterings inside the positive energy band, whose effective scattering potential is

$$\hat{V}^{(11)}_{\vec{k},\vec{k}'}=V_0\left[\cos\frac{\theta_{\vec{k}}}{2}\cos\frac{\theta_{\vec{k}'}}{2}+\sin\frac{\theta_{\vec{k}}}{2}\sin\frac{\theta_{\vec{k}'}}{2}e^{i(\phi_{\vec{k}}-\phi_{\vec{k}'})}\right]. \tag{6}$$

This effect also appears in the QPI analysis of the orbital-band systems where orbital hybridization brings strong momentum dependence to the scattering process.[23]

III. EFFECT OF SPIN ORIENTATION ON THE QPI PATTERN

The points of extremal curvature on the Fermi surface are divided into two groups, arising from the "valleys" ($k=k_L$, positive curvature) and "tips" ($k=k_U$, negative curvature). We define the complexified points $A=k_Le^{i\pi/3}$, $B=k_L$, $C=k_Le^{-i\pi/3}$, $W=k_Ue^{5\pi i/6}$, $X=k_Ue^{-5\pi i/6}$, and $Y=k_Ue^{-i\pi/2}$. Then from Eq. (6) we obtain $|V^{(11)}_{AB}|^2=\frac{3V_0^2}{4}\sin^2\vartheta$, $|V^{(11)}_{AC}|^2=\frac{V_0^2}{4}+\frac{3V_0^2}{4}\cos^2\vartheta$, and $V^{(11)}_{A\bar{A}}=0$, where $\bar{A}=-A$, corresponding to scattering through the vectors $\vec{q}_3$, $\vec{q}_2$, and $\vec{q}_1$, respectively, with $\tan\vartheta=(k_c/k_L)^2$. We also find $|V^{(11)}_{WX}|^2=\frac{3V_0^2}{4}$, $|V^{(11)}_{WY}|^2=\frac{V_0^2}{4}$, and $V^{(11)}_{W\bar{W}}=0$. These processes are depicted in Fig. 1(a).

While $V^{(11)}_{A\bar{A}}=V^{(11)}_{W\bar{W}}=0$ is a direct consequence of TR symmetry, the other processes through scattering vectors $\vec{q}_{2,3,5,6}$ are in general finite. Their amplitude variation may be understood in terms of the spin orientation of the eigenfunctions throughout the Brillouin zone, $\vec{S}(\vec{k})=(-\sin\theta_{\vec{k}}\sin\phi_{\vec{k}},\sin\theta_{\vec{k}}\cos\phi_{\vec{k}},\cos\theta_{\vec{k}})$, depicted in Fig. 1(b). Bi_2Te_3 has the symmetry of C_{3v}, i.e., threefold rotational symmetry plus the three reflection lines (Γ-M plus two equivalent lines). Therefore at the tips $S^z(\vec{k})$ must vanish since σ^z is odd under the mirror operation. $S^z(\vec{k})$ has the largest magnitude at the valleys, but with staggered signs, as shown in the figure. Since scalar-potential scattering does not flip electron spin, its matrix element is largest when $\vec{S}(\vec{k})\cdot\vec{S}(\vec{k}')$ is large and positive, i.e., high spin overlap. This echoes the experimental finding of Pascual *et al.*[24] that in the QPI pattern on Bi(110), only the scattering processes preserving the spin orientation are visible. One major difference, however, betwwen Bi(110) and Bi_2Te_3 is that the former has multiple Fermi surfaces and the scattering processes preserving spin orientations do exist at finite $\vec{q}$ while the later only has one Fermi surface and therefore no such scatterings could exist. At the tips, the spin lies in plane, with $\theta_{\vec{k}}=\frac{\pi}{2}$, independent of the scanning energy E. It can be checked that $\vec{S}(\vec{k}+\vec{q}_5)\cdot\vec{S}(\vec{k})>\vec{S}(\vec{k}+\vec{q}_6)\cdot\vec{S}(\vec{k})$, hence $|V^{(11)}_{WX}|^2>|V^{(11)}_{WY}|^2$. For scatterings between the valleys, $\vec{S}(\vec{k})\cdot\vec{S}(\vec{k}')$ depends crucially on $S^z(\vec{k})$ and $S^z(\vec{k}')$. Accounting for the valley-to-valley oscillation in $\vec{S}(\vec{k})$, we conclude that as the scanning energy increases, $|V^{(11)}_{AC}|^2$ grows while $|V^{(11)}_{AB}|^2$ shrinks. This simple argument gives a qualitative explanation for the absence of the $\vec{q}_3$ scattering in the STM experiment.[21] For typical experimental parameters,[17] $E/E^*\approx 1.5$ and $k_L/k_c\approx 1$. In this case we estimate the scalar-potential scattering gives that $|V^{(11)}_{WX}|^2:|V^{(11)}_{AC}|^2:|V^{(11)}_{AB}|^2:|V^{(11)}_{WY}|^2\approx 6:5:3:2$.

IV. NUMERICAL RESULTS

To specifically compute the QPI image, we employ a T-matrix approach[25] for multiband systems.[23] In the operator basis $\Psi(\vec{k})=U(\vec{k})\psi(\vec{k})$, the Green's function is written in matrix form as

$$\hat{G}(\vec{k},\vec{k}',\omega)=\hat{G}_0(\vec{k},\omega)\delta_{\vec{k},\vec{k}'}+\hat{G}_0(\vec{k},\omega)\hat{T}_{\vec{k},\vec{k}'}(\omega)\hat{G}_0(\vec{k}',\omega), \tag{7}$$

where the T matrix satisfies

$$\hat{T}_{\vec{k},\vec{k}'}(\omega)=\hat{V}_{\vec{k},\vec{k}'}+\int d^2p\hat{V}_{\vec{k},\vec{p}}\hat{G}_0(\vec{p},\omega)\hat{T}_{\vec{p},\vec{k}'}(\omega) \tag{8}$$

and $[\hat{G}_{0,\sigma}(\vec{k},\omega)]_{ab}=[\omega+i\delta-E_a(\vec{k})]^{-1}\delta_{a,b}$ are the bare Green's functions. In spectroscopic imaging STM,[25] the conductance (dI/dV) measured by the STM is proportional to the local density of states defined as

$$\rho(\vec{r},\omega)=\rho_\uparrow(\vec{r},\omega)+\rho_\downarrow(\vec{r},\omega), \tag{9}$$

where $\rho_\sigma(\vec{r},\omega)=\mathrm{Im}\,G_\sigma(\vec{r},\vec{r},\omega)$ is the local density of states for spin σ. The QPI image in the Brillouin zone $\rho(\vec{q},\omega)$ is then obtained by performing the Fourier transformation of the conductance dI/dV. As a result, we can calculate $\rho(\vec{q},\omega)$ using the T-matrix formalism by

$$\begin{aligned}\rho(\vec{q},\omega)&=\int d^2re^{i\vec{q}\cdot\vec{r}}\rho(\vec{r},\omega)\\&=\frac{1}{2i}\int d^2k\ \mathrm{Tr}\{\hat{U}(\vec{k})\hat{G}(\vec{k},\vec{k}+\vec{q},\omega)\hat{U}^\dagger(\vec{k}+\vec{q})\\&\quad-[\hat{U}(\vec{k})\hat{G}(\vec{k},\vec{k}-\vec{q},\omega)\hat{U}^\dagger(\vec{k}-\vec{q})]^*\},\end{aligned} \tag{10}$$

where the trace is taken with respect to the matrix index. Because physically STM measures the local density of states in the spin basis of $\hat{\psi}(\vec{k})$ while our T-matrix theory here is developed in the eigenbasis of $\hat{\Psi}(\vec{k})$, the SU(2) rotation matrices $\hat{U}(\vec{k})$ are introduced in the last line of Eq. (10) to transform back to the physical spin basis. Because the first term in Eq. (7), $\rho(\vec{q}=0)$ contains the sum of the total density of states without the impurity, which makes it much larger than $\rho(\vec{q}\neq 0)$, we only plot $|\rho(\vec{q}\neq 0)|$ in order to reveal weaker structures of the QPI induced by the impurity scattering.

We solve Eq. (8) numerically, using 2D polar coordinates. Since the dominant scattering processes are between $\vec{k}$ points on the constant energy contour $E_+(k,\theta)=E$ (we focus on $E>0$ here), we perform the integration within the range $k_L\leq k\leq k_U$ with k_L and k_U indicated in Fig. 1(a). The resulting QPI images are plotted in Fig. 2 for $c=0$ with $E=1.5E^*$ fixed. For this choice of parameters, $k_L/k_c=1.029$ and $k_U/k_c=1.5$. As shown in Fig. 2(a), $\vec{q}_5$ and $\vec{q}_2$ indicated by the red (dark gray) and green (light gray) circles are the strongest features while $\vec{q}_3$ (indicated by the white circle) is almost invisible. The reason why $\vec{q}_5$ is even stronger than $\vec{q}_2$ while they have comparable scalar scattering potential is due to the difference in the density of states. Because the tip points shown in Fig. 1(a) have larger density of states than the valley points, the weights of $\vec{q}_5$ is larger than those of $\vec{q}_2$,

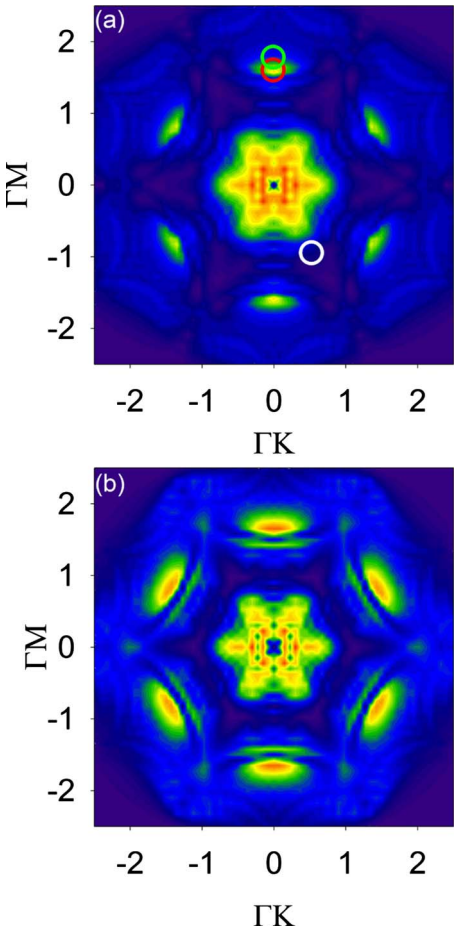

FIG. 2. (Color online) The quasiparticle interference image for (a) $c=0$ and (b) $c=0.5$ with $E=1.5E^*$ and $V_0/E^*=0.1$. In this case, $k_L/k_c=1.029$ and $k_U/k_c=1.5$. (a) The strongest large $\vec{q}$ scatterings are $\vec{q}_5$ and $\vec{q}_2$ indicated by the red (dark gray) and green (light gray) circles (and their symmetric points). $\vec{q}_3$ (indicated by the white circle) is too weak to be seen. (b) For $c=0.5$, new QPI features with large momenta are visible.

resulting in the stronger features observed for $\vec{q}_5$. The strong features near $\vec{q}=0$ correspond to small $\vec{q}$ scatterings around the tips and valleys points, which have also be seen in experiments. Our results reproduce satisfactorily the experimental findings and are also consistent with the analysis from the spin-orientation selection rule discussed above.

As the scanning energy increases further, the surface states along the Γ-M direction start to merge into the conduction band of the bulk states. In this case, the tips of the constant energy contour will be mixed up with these bulk bands, which weakens the $\vec{q}_5$ scattering but enhances the small $\vec{q}$ scatterings near the Γ point. This is consistent with the experiment,[21] showing that the area of the strong features near Γ point becomes much larger after the scanning energy exceeds the bottom of the conduction band.

V. SPIN-ORBITAL SCATTERING IMPURITY

Now we briefly comment on the effect of the spin-orbit scattering given in Eq. (4) which, in principle, exists in any

realistic system. Since surface states of the topological insulator Bi_2Te_3 are two dimensional, the spin-orbit scattering potential only has one component,

$$\mathcal{H}_{\rm imp}^{\rm SO} = icV_0 \int d^2k d^2k' kk' \sin(\phi_{\vec{k}'} - \phi_{\vec{k}}) \psi^\dagger(\vec{k}') \sigma^z \psi(\vec{k}). \tag{11}$$

Backscattering is still forbidden because of the $\sin(\phi_{\vec{k}'} - \phi_{\vec{k}})$ factor. Although σ^z does not flip spin, the angle dependence $\sin(\phi_{\vec{k}'} - \phi_{\vec{k}})$ gives rise to an additional suppression beyond that from the spin-orientation selection rule discussed in the case of scalar impurity scattering. Moreover, because the matrix element is linear in kk', the spin-orbit scattering tends to enhance the scatterings between quasiparticles with large momenta. All these additional effects due to the spin-orbit scattering can be roughly seen in a straightforward calculation froim Eq. (5),

$$|V_{A\bar{A}}^{(11)}|^2 = |V_{W\bar{W}}^{(11)}|^2 = 0,$$

$$|V_{AC}^{(11)}|^2 = \frac{V_0^2}{4}\left[\left(1 - \frac{3}{2}ck_L^2\right)^2 + 3\cos^2\vartheta\left(1 + \frac{1}{2}ck_L^2\right)^2\right],$$

$$|V_{AB}^{(11)}|^2 = \frac{3V_0^2}{4}\sin^2\vartheta\left(1 - \frac{1}{2}ck_L^2\right)^2,$$

$$|V_{WX}^{(11)}|^2 = \frac{3V_0^2}{4}\left(1 - \frac{1}{2}ck_U^2\right)^2,$$

$$|V_{WY}^{(11)}|^2 = \frac{V_0^2}{4}\left(1 - \frac{3}{2}ck_U^2\right)^2. \tag{12}$$

Nonzero c brings in new interferences which could lead to unusual suppressions or enhancements for some scattering wave vectors, depending not only on the magnitude and sign of c but also on the scanning energy E. In Fig. 2(b) we show the QPI image for $c=0.5$. While the main features are still similiar to those of Fig. 2(a), new prominent features associated with larger momentum scatterings are visible. Since the matrix elements for spin-orbit scattering are larger for quasiparticles with larger momentum, this term will become more and more important as the scanning energy E increases. A detailed analysis of the spin-orbit scattering will be presented in a future publication. In comparison with the results in Ref. 21, we find that spin-orbit scattering from the impurity of the Ag atom is not very important in this particular experiment.

VI. CONCLUSION

In conclusion, we have analyzed the quasiparticle interference induced by nonmagnetic impurities on the surface of the topological insulator Bi_2Te_3 using a T-matrix approach. While the backscattering is completely forbidden by time-reversal symmetry, other scatterings are allowed, resulting in the QPI patterns observed in STM experiments.[20,21] We have shown further that the scattering strengths depend crucially on the spin orientations of the eigenfunctions. Since nonmagnetic impurities cannot flip spin, the scalar scattering potential between two eigenstates is larger as their spin overlap is larger. Combined with the variation in the density of states, we have shown that some of the scatterings might be too weak to be seen in comparison with the strongest ones, and our results successfully reproduce the QPI patern observed in experiments. We have further discussed the effect of the spin-orbit scattering on the QPI pattern. While the backscattering is still forbidden, we find that the spin-orbit scattering enhances several new features at large momentum, and the detailed QPI features strongly depends on the sign and strength of the spin-orbit scattering potential.

Note added. While this paper was about completion, we learned a related work by Zhang *et al.*[26]

ACKNOWLEDGMENTS

We are grateful to Xi Chen, Liang Fu, Aharon Kapitulnik, Qin Liu, Xiaoliang Qi, Qikun Xue for insightful discussions. C.W. and W.C.L. are supported by ARO-W911NF0810291. S.C.Z. is supported by the Department of Energy, Office of Basic Energy Sciences, Division of Materials Sciences and Engineering, under Contract No. DE-AC02-76SF00515.

[1] B. A. Bernevig, T. L. Hughes, and S.-C. Zhang, Science **314**, 1757 (2006).
[2] C. L. Kane and E. J. Mele, Phys. Rev. Lett. **95**, 146802 (2005).
[3] B. A. Bernevig and S.-C. Zhang, Phys. Rev. Lett. **96**, 106802 (2006).
[4] X. L. Qi, T. L. Hughes, and S. C. Zhang, Phys. Rev. B **78**, 195424 (2008).
[5] L. Fu and C. L. Kane, Phys. Rev. B **76**, 045302 (2007).
[6] J. E. Moore and L. Balents, Phys. Rev. B **75**, 121306(R) (2007).
[7] R. Roy, arXiv:cond-mat/0607531 (unpublished).
[8] H. Zhang, C.-X. Liu, X.-L. Qi, X. Dai, Z. Fang, and S.-C. Zhang, Nat. Phys. **5**, 438 (2009).
[9] M. König, S. Wiedmann, C. Brune, A. Roth, H. Buhmann, L. W. Molenkamp, X.-L. Qi, and S.-C. Zhang, Science **318**, 766 (2007).
[10] D. Hsieh, D. Qian, L. Wray, Y. Xia, Y. S. Hor, R. J. Cava, and M. Z. Hasan, Nature (London) **452**, 970 (2008).
[11] Y. Xia, D. Qian, D. Hsieh, L. Wray, A. Pal, H. Lin, A. Bansil, D. Grauer, Y. S. Hor, R. J. Cava, and M. Z. Hasan, Nat. Phys. **5**, 398 (2009).
[12] Y. L. Chen *et al.*, Science **325**, 5937 (2009).
[13] P. Roushan, J. Seo, C. V. Parker, Y. S. Hor, D. Hsieh, D. Qian, A. Richardella, M. Z. Hasan, R. J. Cava, and A. Yazdani, Nature (London) **460**, 1106 (2009).
[14] C. Wu, B. A. Bernevig, and S.-C. Zhang, Phys. Rev. Lett. **96**, 106401 (2006).

[15] C. Xu and J. E. Moore, Phys. Rev. B **73**, 045322 (2006).
[16] D. Hsieh, Y. Xia, L. Wray, D. Qian, A. Pal, J. H. Dil, J. Osterwalder, F. Meier, G. Bihlmayer, C. L. Kane, Y. S. Hor, R. J. Cava, and M. Z. Hasan, Science **323**, 919 (2009).
[17] L. Fu, arXiv:0908.1418 (unpublished).
[18] T. Hanaguri, Y. Kohsaka, J. C. Davis, C. Lupien, I. Yamada, M. Azuma, M. Takano, K. Ohishi, M. Ono, and H. Takagi, Nat. Phys. **3**, 865 (2007).
[19] Q.-H. Wang and D.-H. Lee, Phys. Rev. B **67**, 020511(R) (2003).
[20] Z. Alpichshev, J. G. Analytis, J. H. Chu, I. R. Fisher, Y. L. Chen, Z. X. Shen, A. Fang, and A. Kapitulnik, arXiv:0908.0371 (unpublished).
[21] T. Zhang, P. Cheng, X. Chen, J.-F. Jia, X. Ma, K. He, L. Wang, H. Zhang, X. Dai, Z. Fang, X. Xie, and Q. Xue, arXiv:0908.4136 (unpublished).
[22] K. K. Gomes, W. Ko, W. Mar, Y. Chen, Z.-X. Shen, and H. C. Manoharan, arXiv:0909.0921 (unpublished).
[23] W.-C. Lee and C. Wu, Phys. Rev. Lett. **103**, 176101 (2009).
[24] J. I. Pascual, G. Bihlmayer, Yu. M. Koroteev, H.-P. Rust, G. Ceballos, M. Hansmann, K. Horn, E. V. Chulkov, S. Blugel, P. M. Echenique, and Ph. Hofmann, Phys. Rev. Lett. **93**, 196802 (2004).
[25] A. V. Balatsky, I. Vekhter, and J.-X. Zhu, Rev. Mod. Phys. **78**, 373 (2006).
[26] X. Zhou, C. Fang, W.-F. Tsai, and J. Hu, arXiv:0910.0756 (unpublished).